Curvature-induced hydrophobicity at imogolite-water interfaces

Alejandro Fernandez-Martinez, Jinhui Tao, Adam F Wallace, Ian C Bourg, Mark R Johnson, James J de Yoreo, Garrison Sposito, Gabriel J Cuello, Laurent Charlet

Curvature-induced hydrophobicity at imogolite-water interfaces

Alejandro Fernandez-Martinez,*[a] Jinhui Tao, [b] Adam F. Wallace, *[c] Ian C. Bourg, *[d] Mark R. Johnson, [e] James J. De Yoreo,[b,f] Garrison Sposito, [g] Gabriel J. Cuello, [e] and Laurent Charlet [a]

Imogolite, a nanotubular aluminosilicate mineral, is commonly found in volcanic soils, where it exerts a control on carbon dynamics. Synthetic imogolites are used for the removal of contaminants from industrial effluents and are considered for a range of other applications including gas adsorption and functionalised heterogeneous catalysts. In spite of their environmental and industrial relevance, the properties of imogolite-water interfaces remain poorly understood. Here, an experimental and computational study is presented in which the structure and energetics of water are characterized on the curved external surface of imogolite and the hydrophilicity of this surface is contrasted with that of gibbsite, its planar counterpart. Atomic force spectroscopy experiments show that in spite of their identical surface structure, imogolite has a lower hygroscopicity than gibbsite. Molecular dynamics simulations provide an explanation for this observation: the curvature of imogolite prevents the formation of in-plane H-bonds along the directions of the nanotube circumference, lowering the enthalpy of adsorption of water molecules. The different arrangement of surface H-bonds and the resulting differences in hydration properties also affects the acidity constants of surface hydroxyl groups. This 'nanotube effect' may be relevant to other nanotubular systems with high curvatures, potentially impacting their wetting properties, their colloidal stability and their affinity towards hydrophobic organic moieties.

Introduction

The affinity of water for mineral surfaces controls many fundamental processes in nature at different spatial and temporal scales. Examples include the multiphase flow of water and non-aqueous fluids (such as air, hydrocarbons, or supercritical CO_2) in geologic systems,[1] the nucleation and growth of biominerals in living organisms,[2] the formation of mineral-organic aggregates in soils,[3] and the uptake of water vapour by mineral dust aerosols.[4] In these situations and others, observed macroscopic-scale properties are fundamentally grounded in the hygroscopicity of the mineral surfaces and, in particular, in the affinity adsorbed water molecules and thin films for the mineral-air interface.

In spite of the importance of the phenomena outlined above, the fundaments underlying the stability of adsorbed water on mineral surfaces remain incompletely understood. One reason for this lack of clarity is the scarcity of studies comparing the atomistic-level structure and energetics of water on different mineral surfaces. Studies based on interferometry,[5] ellipsometry,[6] and gravimetric adsorption measurements[7] have established a relatively extensive dataset on the adsorption of water on a range of mineral surfaces, but these techniques provide only a macroscopic, averaged view of the films. Conversely, studies based on infrared spectroscopy,[8–10] frequency-modulation atomic force microscopy,[11] or atomistic simulations [i.e., molecular dynamics (MD),[12] Monte Carlo (MC),[13] or density functional theory (DFT) simulations] have produced detailed nanoscale views of adsorbed water on mineral surfaces but have focused on a relatively small number of surfaces, most predominantly the basal surface of muscovite mica.

To date, only a few studies have compared water adsorption on a range of different mineral surfaces using techniques that provide atomistic-level information. Wang et al. (2006)[14] used MD simulations to compare the enthalpy and microstructural details of adsorbed water films on the basal surfaces of five layered minerals with different surface charge and surface hydroxyl densities (brucite, gibbsite, hydrotalcite, muscovite, and talc); Rotenberg et al. (2011)[15] used MD simulations to compare the free energy, microstructure, and larger-scale wettability features (e.g., partial wetting) associated with water adsorption on the basal surfaces of three uncharged layered minerals with a subtle structural difference: the presence and orientation of a hydroxyl group buried ~3 Å within the mineral (pyrophyllite, talc, and fluorotalc). These two studies of adsorption on minerals, combined with insights from studies of water adsorption on other surfaces such as metals[16] or carbon nanotubes,[17] reveal that mineral hygroscopicity is determined by multiple factors including the presence and localization of surface charge sites and associated adsorbed counterions (that can act as binding centres for water molecules), the presence and density of hydroxyl groups (that can donate hydrogen bonds to adsorbed water molecules), and the spatial distribution of surface hydroxyls at the mineral-water interface (that can facilitate or hinder interactions between adsorbed water molecules).

A second reason for the lack of clarity outlined above is that adsorbed water films are inherently two-dimensional phases: their scale is atomistic in the direction normal to the surface but macroscopic in other directions. Therefore, their stability is sensitive to both specific short-range interactions with the surface and collective long-range phenomena such the ability of water molecules to collectively solvate adsorbed counterions and capillary effects due to surface curvature and interfacial energies. This sensitivity to both specific short-range and collective long-range interactions is confirmed by recent studies. However, it is not captured by the predominant theoretical frameworks used to describe adsorbed water films,

as these assume the predominance either of short-range interactions with the mineral surface (as in the case of the well-known Brunauer–Emmett–Teller theory) or of long-range collective effects (as in the case of the Frenkel-Halsey-Hill, Derjaguin-Landau-Verwey-Overbeek, and Köhler theories).[4,7]

In the present study, we approach the challenges outlined above by characterizing and contrasting the hygroscopicities of two natural mineral surfaces: the external surface of imogolite nanotubes and the basal surface of gibbsite nanosheets. These two minerals present isostructural oxyhydroxide surfaces with one key difference: the imogolite external surface is convex, whereas the gibbsite basal surface is planar (Fig. 1). To our knowledge, such a comparative examination of two surfaces of unequal curvature has only been used in one previous study of water adsorption (on a concave hydrophobic surface) which showed results consistent with continuum scale descriptions based on the Kelvin equation.[18] It has not yet been applied to either a convex or a hydrophilic surface and should provide insight into the relative importance of short- vs. long-range effects in controlling film stability. Our approach relies on a combination of experimental and atomistic simulation techniques that provide complementary atomistic-level views of water adsorption, namely MD simulations and atomic force spectroscopy measurements. We note that our study does not directly examine macroscopic manifestations of hydrophilicity such as the contact angles formed by water droplets (which have a complex relationship to the microscopic properties of interfacial water)[15] although it does establish a basis for future studies of these properties.

Beyond their utility to help resolve the fundamental questions outlined above, the systems investigated here have important implications in soil science (where gibbsite and imogolite are among the most important minerals in highly weathered soils such as boreal rainforest and volcanic ash soils)[19] and in materials science (for example, in the synthesis of nanocomposite materials based on imogolite-like nanotubes).[20,21]

Materials and methods

Imogolite and Gibbsite

Imogolite ($Al_2(OH)_3SiO_3OH$) is an aluminosilicate mineral commonly found in the clay fractions of volcanic ash soils and spodosols.[19,22–26] It has a high specific surface area (> 400 m^2/g)[27] and is known to strongly impact the fate and transfer of metals[28–30] and natural organic matter in the soils in which it is found.[31] It has a nanotubular geometry, with an internal face dominated by silanol (>$SiOH^0$) functional groups and an external face composed by a curved gibbsite-like sheet ($Al(OH)_3$) with neutral aluminol functional groups (>Al_2OH^0) (Fig. 1).[32,33] The nanotubes have internal and external diameters on the order of 1 nm and 2.2 nm, respectively, and lengths of up to ~1000 nm.[34,35] The presence of amphoteric surface sites and the lack of isomorphic substitutions make imogolite a mineral with a variable (pH-dependent) charge,[36] although some studies have reported that the external surface may carry a permanent negative charge resulting either from vacancies in the crystal structure or from a curvature-induced undersaturation of surface O atoms.[27,37,38]

Gibbsite ($Al(OH)_3$) is a planar mineral present in bauxitic deposits and widespread in weathered soils. Its structure is composed of H-bonded dioctahedral layers, with the same stoichiometry as the external layer of imogolite.

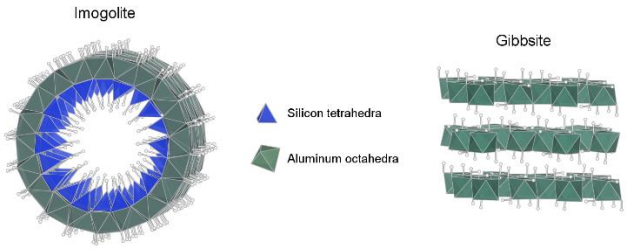

Figure 1 Atomistic views of imogolite and gibbsite. The external surface of imogolite has a curved gibbsite-like (001) structure. The white spheres are H atoms in surface hydroxyl groups, which are drawn perpendicular to the surface in this representation. The orientations of gibbsite OH surface groups are the same as in bulk gibbsite as reported by Balan et al. (2006)[39].

Computational studies

Models of the gibbsite-water interface were constructed by cleaving a gibbsite structure along the (001) plane[40] to create a system containing two gibbsite layers in a 17.36 × 15.23 × 75 Å ($a \times b \times c$) simulation cell. For imogolite, a single nanotube was constructed in a 50 Å × 50 Å × 25.29 Å simulation cell. The nanotube contained ten molecular $Al_2(OH)_3SiO_3OH$ units along the circumference, based on the reported structure of natural imogolite, with the 'zig-zag' configuration.[32,33] A simulation cell of bulk liquid water was also simulated containing 256 water molecules (with no mineral). In total, the models of gibbsite and imogolite contained 72 and 180 surface OH groups, respectively.

The ClayFF model was used in all MD simulations. ClayFF is an interatomic potential model whose Hamiltonian includes Coulomb interactions between fixed-charge atoms and a 6-12 Lennard-Jones representation of Van der Waals interactions, a bond stretching term for surface and water OH bonds, and a three-body angular term to reproduce water angle bending modes.[41] Gibbsite was one of the minerals used to parametrize ClayFF, and thus its structure is reproduced with high accuracy: the difference with the experimental lattice constant being less than 4.1%.[14] The structure of imogolite is also reproduced with high fidelity.

The ClayFF model was originally developed for use with the SPC water model. This combination of models has been extensively used to evaluate water structure and properties and for the interaction of water with hydroxide mineral surfaces, including imogolite.[14,41–45] In addition, the ClayFF model, when used with the slightly different SPC/E water model, has been repeatedly reported to give excellent predictions of the properties of water

on mineral surfaces.[46,47] Relative to the SPC/E model, the original SPC model produces somewhat less accurate prediction of water structure and dynamics,[43] but a more accurate prediction of the enthalpy and free energy of vaporization of liquid water.[48] As shown below, the SPC model successfully reproduces the two adsorption sites for water molecules at the gibbsite (001) surface reported by Veilly et al. (2008) using density functional theory methods.[49]

Molecular dynamics simulations were performed in the canonical ensemble (*NVT*) using the program LAMMPS.[50] The structures of the dry surface models were relaxed during 0.5 ns equilibration runs. Each hydrated system was then prepared by loading the equilibrated dry surface model with a specified number of randomly placed water molecules. Following surface loading, the mineral structure was held stationary as the solvent was relaxed for 0.5 ns, after which the entire hydrated structure (mineral and solvent) was relaxed for an additional 1.0 ns. Simulations were performed on the NERSC supercomputer Franklin and on the University of Delaware's Caviness Cluster. Analyses of the trajectories were performed using custom-made codes written in Fortran 95 and Python.

Helmholtz free energies of hydration (ΔF) were calculated from the enthalpy (ΔH) and entropic (ΔS) changes associated with water adsorption:

$$\Delta F(\phi) = \Delta H(\phi) - T\Delta S(\phi) \quad \text{eq. (1)}$$

where the surface coverage, ϕ, is defined as the total number of water molecules normalized to the number of O atoms on the hydrated surface (e.g., the external surface of imogolite). Reported potential energies and entropies of hydration were derived using the following expression:[51]

$$\Delta X(\phi) = \frac{\langle X(N)\rangle - \langle X(0)\rangle}{N} - X_b \ \{X = H, S\} \quad \text{eq. (2)}$$

where $X(N)$ is the potential energy or entropy of the wet system, containing N water molecules, $X(0)$ is the potential energy or entropy of the dry system and X_b is the potential energy or entropy of a water molecule in bulk water. The resulting values correspond to the free energy, enthalpy, and entropy of reaction associated with transferring ϕ monolayers of water from bulk liquid water to the dry mineral surface, normalized to the number of transferred water molecules. As reported by Smith (1998),[51] the value of the enthalpic component can be approximated from the ensemble average of the system potential energy, which was computed here from 2.0 ns production runs. Addition of the kinetic energy to the enthalpic component does not result in significantly different results. Entropies were derived by analysing the vibrational density of states within the framework of the Two-Phase Thermodynamic Method (2PT)[52] as implemented in an in-house code. The total system entropy was taken as the sum of the mineral and solvent entropies. For the solvent component, the translational, rotational, and internal vibrational states of each water molecule were considered in the determination of the 2PT entropy.[53] The entropy of the mineral component was derived by summing the translational entropies of each atom type contained within the mineral structure. Values of the specific free energy, enthalpy, and entropy of bulk water were calculated from a simulation cell containing 256 water molecules (with no mineral).

In addition to the MD simulations described above, DFT geometry optimizations of the hydrated structures (with one water layer) of imogolite and gibbsite were performed using the Vienna Ab-initio Simulation Package (VASP).[54,55] The imogolite model used in these ab-initio calculations consisted of one imogolite unit cell with dimensions 35 Å × 35 Å × 8.43 Å. A vacuum gap of 15 Å was placed between the periodical images along the *a* and *b* directions, the tube being periodic along the *c* direction. A supercell of gibbsite containing 2 × 3 unit cells along the *a* and *b* directions (17.37 Å × 15.23 Å × 75 Å) and two layers of gibbsite (001) planes separated by a vacuum layer of 67 Å were used. The calculations were performed at the Gamma point (k = 0), using projector augmented wave (PAW) pseudopotentials (Kresse and Joubert, 1999) with a plane wave cutoff of 209 eV and the Perdew-Burke-Ernzerhof (PBE) functional of the generalized gradient approximation (GGA).[56,57]

Experimental sample description, synthesis, and preparation

A sample of gibbsite [$Al(OH)_3$)] powder was kindly provided by Alcoa Corp (Aviles, Spain). Synthetic aluminosilicate imogolite-like nanotubes [$Al_2(OH)_3SiO_3OH$] were synthesized following the procedure described by Denaix et al. (1999).[58] Aluminum nitrate (99.999%, Alfa Aesar) and Tetraethyl orthosilicate (99.999%, Alfa Aesar) were mixed in ultrapure water at an Al/Si ratio of 2 and aluminium concentration of 0.002 M. Dilute NaOH (0.1 M) was injected at a rate of 2 mL/min under vigorous stirring until reaching a hydrolysis ratio OH/Al of 1. After injection, the solution was stirred for 12 h to avoid the polymerization of Al hydroxides. The solutions were heated at 95°C during five days in closed Teflon bottles. To remove excess alcohol and Na^+ and NO_3^- ions from solution, the solutions were dialyzed against ultrapure water for 15 days using a molecular weight cut-off membrane of 2000 Da (Spectra/Por® membranes, Carl Roth). After dialysis, part of the imogolite solution was freeze-dried and used for the experiments.

The resulting powder was characterized using transmission electron microscopy (TEM) and Fourier transform infrared spectroscopy (FTIR) and showed good agreement with the expected features of synthetic imogolite (see Supporting Information Figures S1 and S2). TEM investigations were carried out on a Philips CM 200 microscope operating at 200 kV. Prior to observation, the powders were immersed in an aqueous chloroform solution. A droplet of this solution was deposited on a copper grid. TEM observations were made after evaporation of the solvent. FTIR spectra of the imogolite freeze-dried powders were taken to characterize the product obtained after the synthesis. Transmission FTIR spectra were obtained using a Bruker HYPERION 3000 FTIR microscope in transmission mode on KBr pellets (1 mg of imogolite in 100 mg of KBr). One hundred scans taken using a resolution of 2 cm^{-1} were averaged to obtain spectra in the range 4000–370 cm^{-1}.

Force spectroscopy

Force spectroscopy measurements were performed using SiOH-terminated tips under ultrapure water to directly probe the interaction between SiOH and the interfacial water or solid surface. Based on previous studies, the free energy measured by DFS probes the sum of SiOH-interfacial water hydrogen bond strength decrease and interfacial water entropy increase during H-bond rupture by pulling the silicon tip away from the gibbsite or imogolite surface.[59,60] Although we do not expect to directly measure the free energy of water adsorption on these two minerals due to the chemical difference between SiOH and HOH, this method gives the most straightforward way to evaluate the relative affinity between water and mineral with surface specificity, which is proportional to hydrophilicity. The main assumption made here is thus that the interaction of a hydroxylated AFM tip with an oxide surface is a reasonable first-order proxy for the attachment of a water molecule at the surface.[59,61–65] To that end, aliquots of synthetic imogolite and gibbsite suspensions were deposited onto muscovite mica disks and dried under N_2. The disks were mounted on a fluid cell for analyses. Tip functionalization (hydroxylation) was performed by plasma cleaning of Si tips on Si_3N_4 AFM cantilevers (Bruker, SNL-10, CA) for 2 min (see Fig. 1a). Measurements were made with the MFP-3D Atomic Force Microscope (Asylum Research, Santa Barbara, CA). To account for any surface heterogeneity, a custom routine randomly sampled points on the surface to give a representative average. A constant approach velocity of 1.04 µm/s was used for every pulling speed studied. An 8 nm deflection trigger was used to contact the surface and dwell for 1 s before pulling away. The AFM tip was vertically retracted from the substrate at five different pulling rates: 651 nm/s, 1040 nm/s, 1740 nm/s, 2600 nm/s and 3910 nm/s. The value of the cantilever spring constant was determined by deflection sensitivity and thermal fluctuation measurements.[66] The collected force versus separation curves typically exhibited a characteristic single rupture event. Curves showing more than one bond breaking event were discarded. We cannot exclude that multiple bond-breaking events are confounded within a single curve. This remains a limitation of the technique.

The approximate analytical expression for the mean rupture force for a single bond is:[60,67,68]

$$\langle f \rangle = \frac{\Delta G}{\nu x_t}\left\{1 - \left[\frac{k_B T}{\Delta G}\, ln\, \frac{k_u^0 e^{\frac{\Delta G}{k_B T}+\gamma}}{\frac{x_t}{k_B T}\frac{df}{dt}}\right]^{\nu}\right\} \quad \text{eq. (3)}$$

where $\langle f \rangle$ is the mean rupture force for a single bond at any loading rate; ΔG is the equilibrium free energy of binding $\Delta G = G_u - G_b$ of the bonded system, G_b, relative to the free cantilever G_u; x_t is the distance between the free-energy minimum and the transition state; ν depends on the shape of the potential energy well (ν = 2/3 for a linear-cubic potential, ν = 1/2 for a harmonic potential, and ν = 1 recovers the phenomenological Bell theory); k_B is the Boltzmann constant; T is absolute temperature; k_u^0 is the intrinsic rate coefficient for the system in absence of applied force; γ = 0.577 is the Euler-Mascheroni constant; and *df/dt* is the loading rate. The energy ΔG of the tip-substrate interaction can be calculated from data on $\langle f \rangle$ vs. *df/dt*.

Results and discussion

Hydration energies: force spectroscopy and molecular dynamics

Fig 2 shows results of the force spectroscopy experiments. Fig. 2b shows the rupture force between the hydroxylated Si (SiOH) tip and the gibbsite or imogolite surface as a function of loading rate. The solid curve in Fig. 2 is a fit to the data according to the theoretical dependence of the bond rupture force on the loading rate (eq. 3). Equilibrium free energies of binding for the SiOH-gibbsite (001) and SiOH-imogolite systems are reported in Table 1. The energy range of the bonds formed between the hydroxylated tip and the surface falls within the expected range for water H-bonds.[69,70] The ΔG value for imogolite is larger than that for gibbsite by 4.41 k_BT (10.92 kJ/mol), which implies that the gibbsite (001) face forms more stable interactions with SiOH groups (and hence potentially also with water molecules). Representative examples of force *vs.* distance curves are shown in Fig. S3.

In order to understand the origin of this difference between the two systems, a series of molecular dynamics simulations were performed with different levels of hydration. Values of the average free energy of hydration per water molecule are shown in Fig. 3. All the values of the average free energy of hydration are negative, indicating that the dry mineral surface is more hygroscopic than bulk liquid water. In other words, both surfaces should carry an adsorbed water film when exposed to ambient water-saturated air. As expected, all curves approach zero (i.e., the energetics of water in the film become more bulk-liquid-like) with increasing film thickness. The lower affinity of water for the curved imogolite surface as compared to the planar gibbsite surface is confirmed by the simulations: almost all the points of the free energy curves, in particular those at low surface coverages, are above the values for gibbsite. Interestingly, a minimum value is observed for both surfaces in the average enthalpy of hydration, but this minimum is positioned at different ϕ values for imogolite ($\phi \sim 1$) and gibbsite ($\phi \sim 0.6$). The origin of these differences is further explored below through detailed analyses of the interactions between surface hydroxyl groups and interfacial water molecules (Fig. 4). We note here that the analysis of the adsorption energies provided above reflect the stability of the entire adsorbed water films (i.e., reported energetics are a collective property emerging from the network of H-bonds at the interfaces). Analyses of adsorption energies of individual water molecules are beyond the scope of this manuscript.

Table 1 Fitted parameters of the interaction model between the SiOH tip and the gibbsite (001) and imogolite surfaces. Results were obtained using the harmonic potential approximation to the surface-tip interaction (i.e., v = 1/2 in Eq. 4).

Surface	Gibbsite (001)	Imogolite external
$k_u^0\ (s^{-1})$	3.78 ± 1.43	74.43 ± 13.37
$x_t\ (nm)$	0.13 ± 0.02	0.10 ± 0.02
$\Delta G\ (k_BT)$	-7.88 ± 0.14	-3.47 ± 0.27

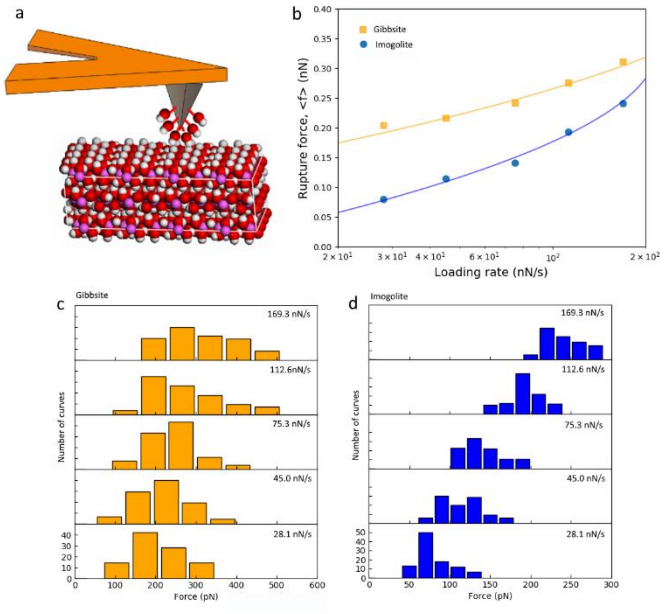

Figure 2 Determination of the equilibrium Gibbs energy of binding of the SiOH tip to the gibbsite and imogolite surfaces. (a) Schematic view illustrating the SiOH tip placed directly on the solid surface. (b) Dynamic force spectra for the rupture of bonds between the tip and the gibbsite (001) or imogolite surfaces (spring constant of 43.30 pN/nm). The solid curves are fit to the data using Eq. 3. (c-d) Histograms of bond rupture forces measured from repeated force–distance trajectories for gibbsite (c) and imogolite (d). Normalized histograms for increasing loading rate (28.1, 45.0, 75.3, 112.6 and 169.3 nN/s) are offset for clarity. The vertical range is 50% for (c) and 60% for (d).

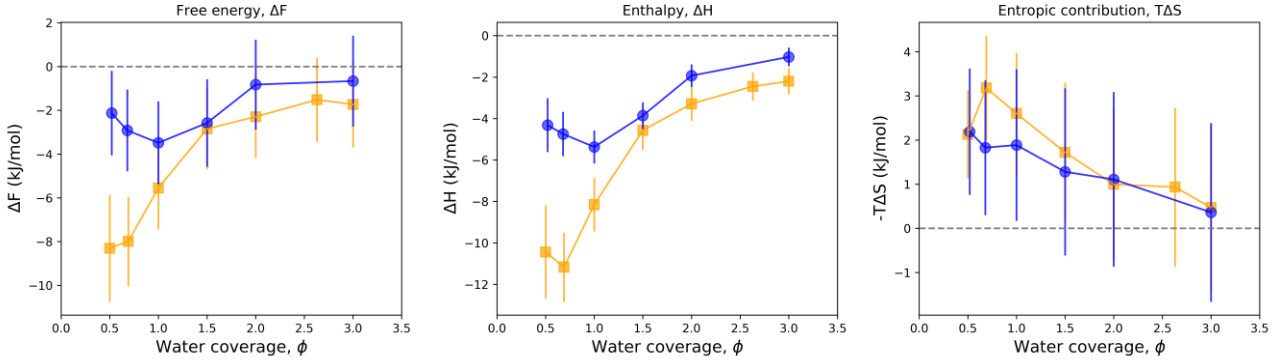

Figure 3 Hydration free energy of imogolite and gibbsite (blue circles and orange squares) as a function of surface coverage (left panel) and its breakdown into enthalpic and entropic components (center and right panels). The results quantify the average (per water molecule) energy associated with transferring ϕ water monolayers from bulk liquid water to the dry mineral surface. The results show that enthalpy favours liquid water uptake on the dry mineral surface, whereas entropic effects inhibit this uptake.

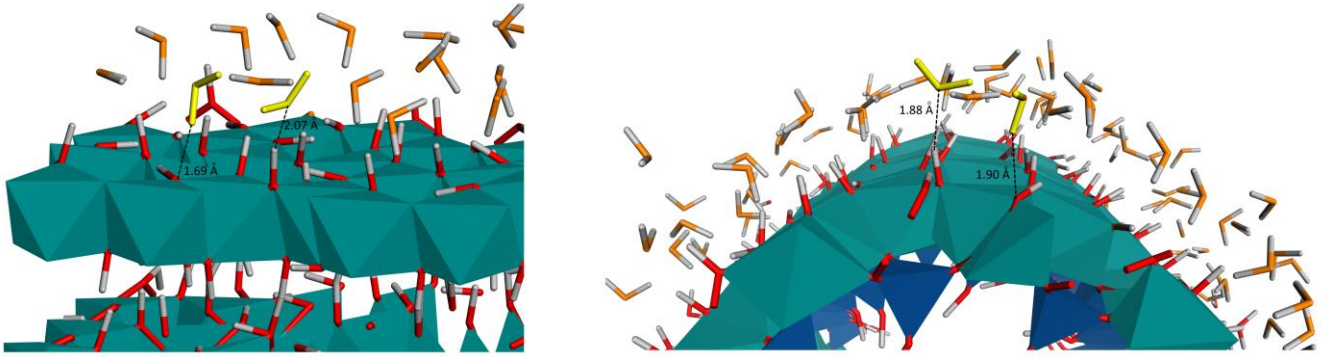

Figure 4 Snapshots of the MD simulations showing H-bonded water molecules in both systems at monolayer coverage (ϕ=1). Left: view of the gibbsite-water interface, showing two water molecules (highlighted in yellow) giving (left) and receiving (right) a H-bond to/from surface hydroxyls. Right: view of the imogolite-water interface with two water molecules (yellow) receiving (left) and giving (right) H-bonds from/to surface hydroxyls.

Orientation of surface hydroxyls. The projections of the O and H atoms from surface hydroxyl groups onto the (001) surface of gibbsite and onto the external surface of imogolite are shown in Fig. 5, together with histograms of the angle β formed between the $\overrightarrow{OH}$ vector of each hydroxyl and the vector normal to the surface for the dry (ϕ=0) and hydrated surfaces (ϕ=4). Histograms for other hydration states are shown in Fig. S4.

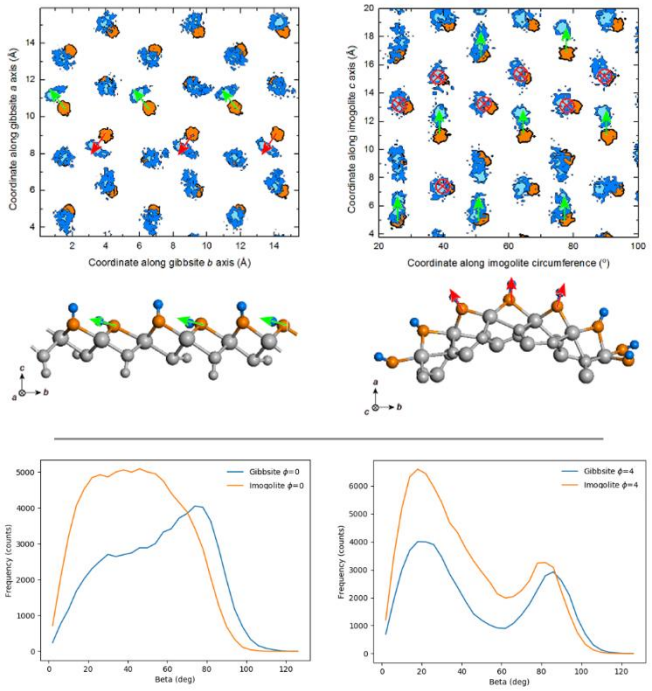

Figure 5 Top: Projections of surface OH groups onto the (001) gibbsite surface (left) and the external imogolite surface (right). The orange circles represent the positions of surface O atoms. The blue regions indicate the more probable positions of hydroxyl H atoms. Red arrows indicate OH groups perpendicular to the surface. Green arrows indicate OH groups parallel to the surface. The position of the empty octahedral site is placed between three O atoms, at the end of the green arrows in the left figure. **Bottom**: histograms showing the distribution of the β angle formed between the OH vector and the normal to the surface for ϕ=0 (left) and ϕ=4 (right).

The histograms show a strong effect of water on the orientations of the hydroxyl groups. The presence of adsorbed water induces an orientation of the surface hydroxyls which is qualitatively similar on both surfaces. The histogram of the β angle for ϕ=4 shows two peaks placed at ~20° and ~85°, i.e., almost 'normal' and almost 'parallel' to the mineral surfaces. A difference between the two surfaces is observed, with a significant higher number of 'normal' hydroxyls in the case of imogolite. The projections in Fig. 5 show differences in the orientations along the *xy* directions (plane of the mineral surfaces): For gibbsite, the OH groups tend to form H-bonds with water or with neighbouring O atoms (towards the empty octahedral site characteristic of its dioctahedral surface structure). On the external imogolite surface, however, the curvature of the nanotube prevents the formation of H-bonds between surface OH groups along its circumference. Thus, only ~1/3 of the OHs are parallel to the surface, with their direction lying along the *c* axis, where there is no curvature.

Structure of adsorbed water at the mineral-water interface. The normalized density profiles of water computed at the gibbsite- and imogolite-water interfaces are shown in Fig. S5. A similar profile, with minima and maxima positioned at similar distances, is observed on both surfaces, indicating that the two surfaces exert similar influence over the structure of adsorbed water. A difference in the width of the first water peak, broader in the case of imogolite, indicates a less ordered first layer, as expected for a less hydrophilic surface.[71] The simplest explanation for this difference is the geometric effect caused by the curvature of the imogolite surface, for example the impact of curvature on the orientation of surface OH groups noted above.

Examination of the angular distributions of water molecules at the surface (Figs. 6 and 7) further suggests that the orientation of surface OH groups strongly influences the properties of adsorbed water. In particular, our calculations reveal the existence of two conformations of adsorbed water on both surfaces. Two angles are needed to describe the orientation of a water molecule. The angle θ is defined between the water dipole vector and the vector normal to the mineral surface, whereas α is the angle between the vector joining the two water hydrogen atoms and a vector normal to the mineral surface. The occurrence of two adsorbed water conformations is most obvious in the distribution of θ angles at low water coverage, where two peaks can be distinguished in the first water monolayer (d ≈ 2.5 Å) of all the histograms: one centred at θ ≈ 122° and the other at θ ≈ 75°. In the case of gibbsite, the peak position of the more acute angle shifts towards lower values as the water coverage increases. The distribution of the α angle is similarly bimodal, particularly at low water coverage, as shown in Fig. 7.

Further examination of the simulation trajectories in light of the angular distributions noted above shows that the first orientation (type A: θ ≈ 120°, α ≈ 45°), corresponds to a water molecule with an OH pointing towards the surface and donating a hydrogen bond to a surface oxygen. The second orientation (type B: θ ≈ 55°, α ≈ 90°) corresponds to a water molecule that accepts a hydrogen bond from the surface (Fig. 4). These two types of adsorbed water were described by Wang et al. (2006) and Veilly et al. (2008) in their investigations of water adsorption on gibbsite.[14,49] Orientation B was shown by Veilly et al. (2008) to be stabilized when two hydroxyl groups participate in the binding. However, although these authors mention the strong hydrogen bonding of orientation A, no comparison is made with the B orientation. On gibbsite, the intensity corresponding to the A orientation (θ≈ 120°) does not increase with increasing water coverage from ϕ = 0.5 to 1.0, meaning that additional first-layer water molecules adsorb on the surface with the B orientation. On imogolite, the same water

orientations are observed,[43] but A orientation does not become saturated until ϕ = 1.0 as shown in the evolution of the peak at $\theta \approx 120°$ between ϕ = 0.5 to ϕ = 1 in Fig. 6. A previous study reported the occurrence of A type water on imogolite, but did not discuss the B type.[43] Instead, a third type was described in which the water dipole vector points away from the surface, and that may occur in positive charged planar regions of the imogolite surface as predicted by the vibrational breathing mode.[43]

The second layer of water molecules on the two mineral surfaces (d ≈ 5 Å) show much less orientational preference than the first layer. On gibbsite, angular distribution maps reveal a minor preference for water molecules orienting one of their OH groups towards the surface ($\theta \approx 130°$, $\alpha \approx 90°$). Again, the effect of curvature is seen in the angular distribution of water molecules in the second hydration shell of imogolite, which is less structured than that of gibbsite.

Water H-bonds with the surface. An analysis of the hydrogen bonding of surface OH groups with water molecules provides further insight into the mechanisms of water adsorption. Histograms of the number of H-bonds donated or accepted by surface OH groups to/from water molecules are shown in Fig. 8. The criteria used to define a hydrogen bond are the following: a water molecule was considered H-bonded if it was located within the first peak of the O-H pair correlation function, which extends to 2.2 Å in the case of a receiving H-bond from water and to 2.3 Å for H-bonds donated to water, similarly to the distances found in a previous study on metal oxides.[72]

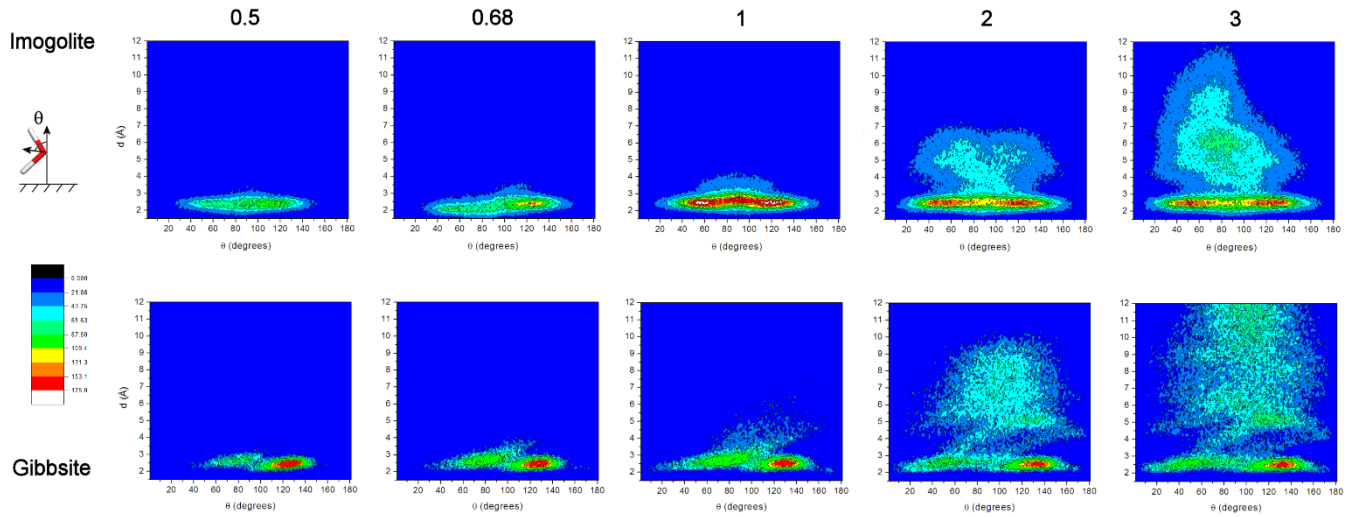

Figure 6 Histograms of the θ orientations of water molecules at the surfaces of imogolite (top) and gibbsite (bottom) as a function of water coverage (numbers at the top). Blue color indicates a low probability of finding a certain orientation, and red represents the maximum probability.

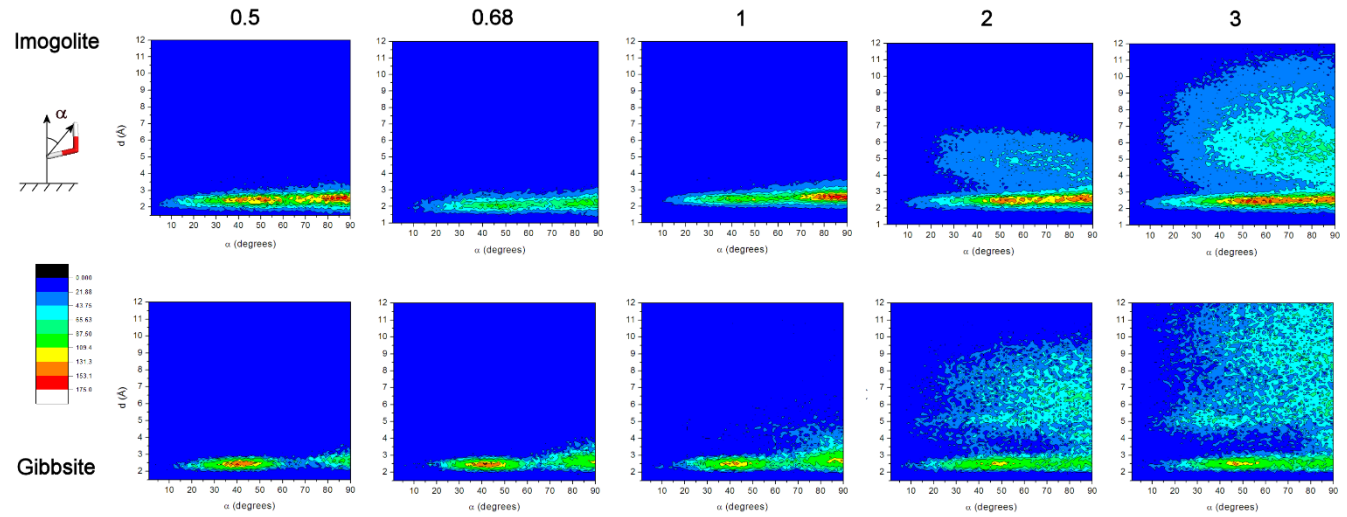

Figure 7 Same as Fig. 6 in the case of the α angle.

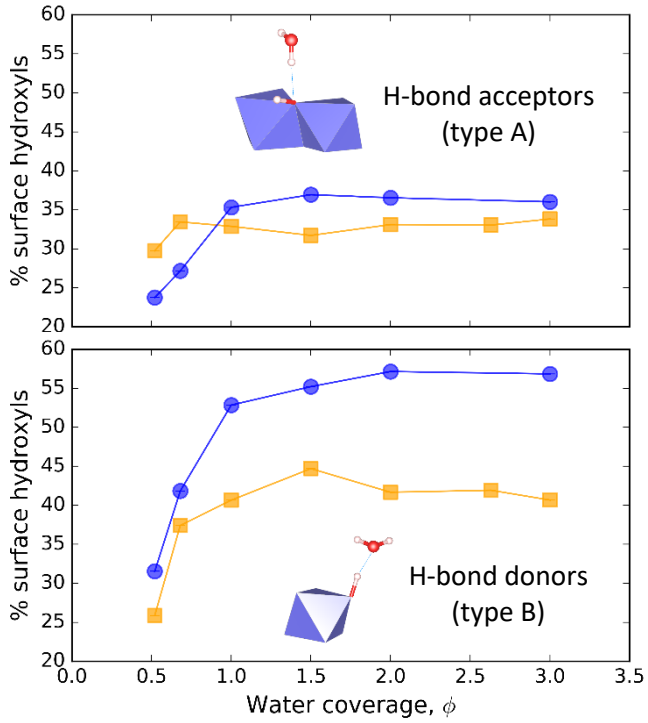

Figure 8 Percentage of surface hydroxyl groups donating or accepting 1 hydrogen bond from water molecules, for both imogolite (blue circles) and gibbsite (orange squares).

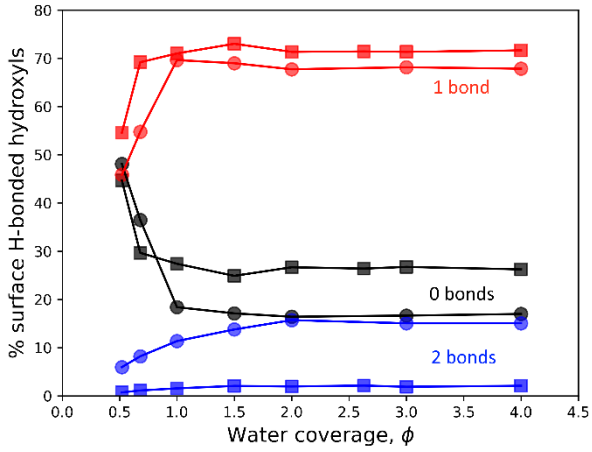

Figure 9 Percentage of surface OH groups forming 0, 1 or 2 H-bonds with water molecules. About a 15% of the sites are able to form two H-bonds with water molecules, in comparison with a 2% in gibbsite. At any instant, a significant number of surface OH groups do not H-bond with water. Squares: gibbsite; Circles: imogolite.

Our results on the number of H-bonds donated and received by surface OH groups are consistent with the orientational distributions shown in Figs. 6-7: the number of hydrogen bond acceptors (water molecules of type A) becomes saturated at $\phi \approx 0.6$ on gibbsite and $\phi \approx 1.0$ on imogolite. On each surface, the water coverage where the type A water population saturates coincides with that where the enthalpy of hydration is most favourable (Fig. 3), suggesting that the surface hydroxyls that are oriented parallel to the surface (Fig. 5) may provide high energy sites for the adsorption of type-A water molecules, and that the greater tendency of surface OH groups to lie parallel to the surface of gibbsite (particularly at low degrees of hydration) may cause the greater affinity of water molecules for this surface.

The percentage of surface hydroxyls forming 0, 1 or 2 H-bonds with water is shown in Fig. 9. It is interesting to note that, although most of the surface OH sites are forming H-bonds, all curves reach a plateau, and that a significant number of surface sites remain 'dry' even at high surface coverage values.

Effect of the curvature on the hydroxyl acidity. To gain additional insight into the impact of surface curvature on surface hydration, we used a bond-valence model approach to characterize the coordination of O atoms on hydrated gibbsite and imogolite surfaces. The bond valence model approach was initially developed to help explain the structures of crystalline minerals[73] and has been extended to help predict the acidity constants of surface OH groups, a key parameter influencing the reactivity of (oxyhydr)oxide surfaces including those examined here.[74,75,76,77] For example, the well-known MUSIC model predicts the pK_a values of surface OH groups using the expression:[75]

$$-pK_a = logK_a = -A\left(\sum_j s_j + V\right) \quad \text{eq. (4)}$$

where V is the valence of oxygen (-2), $\sum_j s_j$ is the sum of the bond valences s_j associated with all the bonds j reaching the oxygen atom, and A = 19.8 is a phenomenological constant. In the case of gibbsite and imogolite, the bond valence sum $\sum_j s_j$ for surface O atoms in $>Al_2OH_0$ functional groups includes the bond valences of the two Al-O bonds and the O-H covalent bond formed by a surface O atom, as well as the bond valence of all H-bonds received by the O atom. The MUSIC model uses a fixed value of s = 0.8 valence units (v.u.) for each covalent O-H bond and s = 0.2 v.u. for each H-bond accepted from a water molecule,[75] such that each additional H-bond received by a surface O atom increases its acidity by 4 pH units. In previous applications of this model to imogolite and gibbsite, Hiemstra and co-workers concluded that $>Al_2OH_0$ functional groups on the gibbsite (001) surface have pK_a values of 0.0 and 11.9, i.e., they are not reactive in the pH range of environmental relevance,[78,79] in agreement with other estimates.[80,81] A previous study of imogolite assumed that the number of H-bonds received by surface O atoms is the same as on gibbsite, such that the acidity constants of both surfaces were predicted to be identical.[27]

Here, instead of assigning a fixed bond valence of 0.2 to each H-bond, we used an alternative approach whereby the bond valence associated with an individual bond decreases with the length of interatomic distance following the relation:[73]

$$s_j = exp\left(\frac{r_0 - r_j}{B}\right) \quad \text{eq. (5)}$$

where r_j is the bond length (including H-bonded water molecules) and r_0 and B are fitted parameters specific of each anion-cation pair. For O-H bonds, values of r_0 and B determined by Brown are shown in Table 2. Equation 5 yields a value of $s_{O\text{-}H}$ that tends asymptotically to zero for large $r_{O\text{-}H}$ values. This allows the bond valence sum $\sum_j s_j$ to be evaluated over all water molecules around a surface site, in contrast to the analysis presented in Figs. 8-9 (where the number of H-bonds was quantified using a distance cut-off value as a criterion). The inclusion of all the water molecules in the bond-valence sum was suggested by Brown (2002), who observed that interactions of water molecules in bulk water placed at long distances from each other should be considered if proper valence sums were to be maintained.[82,83]

Table 2 Parameters used to calculate the bond-valence of surface OH bonds, O…H and O…H_2O hydrogen bonds, using eq. 5.

$r_{O\text{-}H}$ (Å)	r_0 (Å)	B
< 1.05	0.907	0.28
1.05 ≤ $r_{O\text{-}H}$ ≤ 1.70	0.569	0.94
> 1.70	0.99	0.59

Bond valences corresponding to hydrogen bonds formed between surface oxygen atoms and water molecules or surface hydroxyls are reported in Fig. 10 as a function of the surface coverage. The differences between the two systems reflect the influence of the curvature. In Fig. 10, the blue symbols show the bond valence shared by a surface O atom with neighbouring structural H atoms: 0.88 v.u. for gibbsite and 0.83 v.u. for imogolite. This value equals the sum of the bond valence associated with the covalent O-H bond (0.72 v.u. according to Eq. (5) with the parameters from Table 2) and the bond valence associated with H-bonds between surface hydroxyls (0.16 v.u. for gibbsite, 0.11 v.u. for imogolite). In short, surface O atoms on the flat gibbsite surface receive approximated 50% more bond valence from intra-surface H-bonds than O atoms on the curved imogolite surface, in agreement with the greater fractionof OH groups pointing perpendicularly to the surface on imogolite vs. gibbsite.

As shown by the red symbols in Fig. 10, at water coverages greater than one monolayer, the greater tendency of surface O atoms on gibbsite (vs. imogolite) to receive H-bonds from other surface OH groups is partly compensated by their smaller tendency to receive H-bonds from water molecules. At sub-monolayer coverages, however, gibbsite surface O atoms share more bond valence than imogolite surface O atoms with both neighbouring OH groups and with adsorbed water molecules.

In addition to the degree of H-bonding of surface O atoms, values of the protonation constants of the neutral $>Al_2OH_0$ sites calculated by the MUSIC model are very sensitive to small variations of the metal-oxygen bond lengths. In order to obtain these protonation constants using Eq. (4), values for the Al-O bond lengths need to be determined. Different experimental techniques can be used to obtain this information (*e.g.*, Pair Distribution Function, X-ray Absorption Spectroscopy).

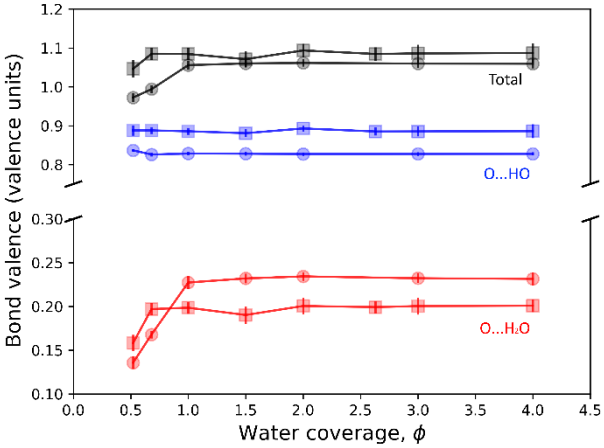

Figure 10 Bond valences of surface oxygen sites resulting from H-bonding with water molecules (red) and with other surface OH groups, plus direct OH bonding (blue). The top (balck) curve indicates the total bond valence received by surface O atoms. Squares: gibbsite; Circles: imogolite.

However, determining the local information about the bonds with surface oxygen atoms remains an experimental challenge. For these reasons, DFT calculations of gibbsite and imogolite–water interfaces were used to obtain an estimation of the average Al-O bond lengths. It is worth noting that the in-plane H-bonding configuration along the axis of the imogolite tube observed for surface hydroxyls groups in classical MD simulations is reproduced by the more accurate DFT calculations (see Fig. S6). In Fig. 10, the Al-O bond lengths ($r_{Al\text{-}O}$) have been plotted as the independent variable, and the $s_{Al\text{-}O}$ bond valences have been calculated using equation (5) with B = 0.37 and r_0 = 1.651 Å.

Both pK_{a1} values follow a trend towards lower values as the Al-O distances increase. The $r_{Al\text{-}O}$ bond lengths obtained from DFT calculations give an estimation of the pK_{a1} for each surface. For imogolite we obtained an average value of $<r_{Al\text{-}O}>$ = 1.95 Å which yields a $pK_{a1\text{-imogolite}}$ = -0.92 ± 0.24. The value obtained for the gibbsite groups is of $<r_{Al\text{-}O}>$ = 1.94 Å, yielding a $pK_{a1\text{-gibbsite}}$ = -0.05 ± 0.50. The acidity constant for imogolite doubly coordinated neutral groups is shifted towards more acidic values by a ΔpK_{a1} = 0.87 ± 0.75. The value for gibbsite is in close agreement with the value reported by Hiemstra et al. (1996) using the CD-MUSIC model (pK_{a1} = 0.0), and in disagreement with other studies, which proposed values of pK_{a1} between 5.2 and 5.9.[80,81]

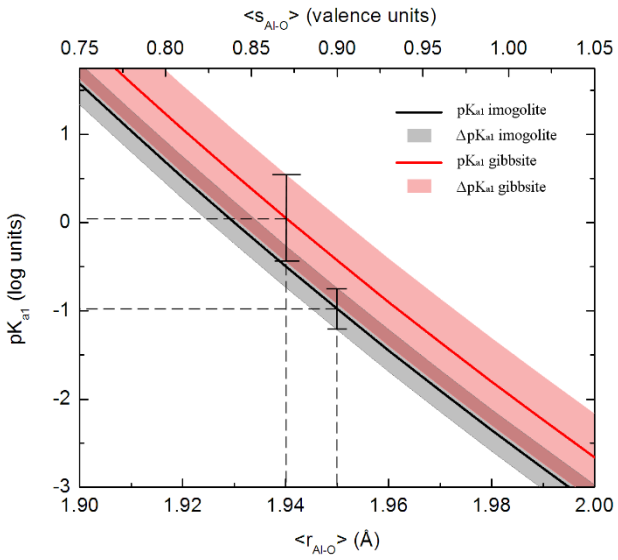

Figure 11 Acidity constants for the surface $>Al_2OH^0$ functional groups calculated using Eq. (5) as a function of Al-O bond length. The scale in the top abscissa indicates the total bond valence due to the two Al-O bonds. The error bars (gray and pink areas) have been calculated from the uncertainties in the s_{O-H} bond valences. An estimation of the absolute acidity constant has been done using $<r_{Al-O}>$ distances obtained from DFT-optimized structures.

Conclusions

The effect of curvature on surface wetting and acidity has been explored using two mineral surfaces with the same surface chemistry, the external curved surface of imogolite and the planar (001) surface of gibbsite. The difference in measured free energy values (7.88 k_BT and 3.47 k_BT) for gibbsite vs imogolite is consistent with our MD simulation predictions of the difference in hydrophilicity between the two minerals. The larger values obtained by AFM vs. MD simulation may reflect a formation of stronger H-bonds by SiOH vs. HOH or the existence of multiple bonds ruptures during the pulling of our AFM tips. The consistency of the experimental and simulation results give us confidence that this methodology is adequate to explore molecular interactions at the mineral-water interface.

A mechanistic explanation of the observed differences in wettability is obtained from analyses of the MD results. These reveal differences in the geometry of water molecules adsorbed within the first hydration layer of the mineral-water interface: whereas gibbsite is able to accept hydrogen bonds from water molecules forming a highly structured first hydration layer (A-type), the curvature of imogolite prevents the formation of some of the H-bonds between surface hydroxyl groups, making the adsorption of water molecules less energetically favourable at sub-monolayer coverages. The different stereo-chemical conditions of water adsorbed on the two systems are further translated into different acidities for surface $>Al_2OH^0$ sites. The results show more acidic pK_{a1} values for doubly-coordinated neutral sites on imogolite than on gibbsite, by $\Delta pK_{a1} = 0.87 \pm 0.75$. The absolute values of the protonation constants reported in this work coincide with those reported by Hiemstra and Van Riemsdijk (1996),[75] who used the same CD-MUSIC model.

The lower hygroscopicity observed for imogolite may be related to several properties that have been classically described as specific to this mineral. Of these, the formation of stable organo-mineral complexes has been largely reported in the soil science literature as a characteristic of soils where imogolite (and other allophanic clays) are present.[31,84–88] The formation of organo–mineral complexes may be facilitated by the high density of functional groups at the surface of imogolite. However, prior to specific interactions with functional groups, the organic molecule has to approach the imogolite surface. The less hydrophilic character of imogolite would be beneficial for this first step, as water is less structured on imogolite surfaces than on other minerals.[14] We note here however that the complexity of soil organic matter and the multiple faces of mineral exposed to the soil solution make organo-mineral interactions complex.[89] The wetting properties studied here are therefore only a part of the puzzle. Further investigations of this property should be made in the future to correctly assess the retention of organic matter by imogolite. Our simulations shed light on another important property of imogolite: its tendency to form bundles. The free energy profile of aggregation of two mineral particles has been shown to depend upon energy barriers related to highly ordered layers of water between the mineral surfaces.[90,91] In the case of imogolite this shell of adsorbed water is less structured, and a lower energy barrier is expected to occur, thus potentially facilitating their aggregation.

Conflicts of interest

There are no conflicts to declare.

Acknowledgements

Barry Bickmore and Kideok K. Kwon are gratefully acknowledged for enriching discussions. Loïc Vidal (Inst. Sciences des Matériaux de Mulhouse, France) is thanked for TEM analyses. A.F.-M. acknowledges the Région Rhône-Alpes for the financial support received through an Explora'DOC fellowship for a 6-months stay at the University of California, Berkeley. 2PT analysis was performed by A.F.W. with support of the U.S. Department of Energy (DOE), Office of Science, Office of Basic Energy Sciences (BES), Chemical Sciences, Geosciences, & Biosciences (CSGB) Division, under Award Number DE-SC0018439. I.C.B. was supported by the U.S. Department of Energy, Office of Science, Office of Basic Energy Sciences, Geosciences Program under Award DE-SC0018419. Molecular dynamics simulations were performed using resources of the National Energy Research Scientific Computing Center (NERSC), which is supported by the U.S. Department of Energy, Office of Science, under Award DE-AC02-05CH11231.

References

1 E. Shahraeeni and D. Or, Pore-scale analysis of evaporation and condensation dynamics in porous media, *Langmuir*, 2010, **26**, 13924–13936.

2 S. Elhadj, J. J. De Yoreo, J. R. Hoyer and P. M. Dove, Role of molecular charge and hydrophilicity in regulating the kinetics of crystal growth, *Proc. Natl. Acad. Sci. U. S. A.*, 2006, **103**, 19237–19242.

3 C. J. Bronick and R. Lal, Soil structure and management: A review, *Geoderma*, 2005, **124**, 3–22.

4 M. Tang, D. J. Cziczo and V. H. Grassian, Interactions of Water with Mineral Dust Aerosol: Water Adsorption, Hygroscopicity, Cloud Condensation, and Ice Nucleation, *Chem. Rev.*, 2016, **116**, 4205–4259.

5 T. E. Balmer, H. K. Christenson, N. D. Spencer and M. Heuberger, The Effect of Surface Ions on Water Adsorption to Mica, *Langmuir*, 2008, **24**, 1566–1569.

6 D. Beaglehole and H. K. Christenson, Vapor adsorption on mica and silicon - Entropy effects, layering and surface forces, *J. Phys. Chem.*, 1992, **96**, 3395–3403.

7 R. M. Pashley, Multilayer adsorption of water on silica: An analysis of experimental results, *J. Colloid Interface Sci.*, 1980, **78**, 246–248.

8 D. B. Asay, A. L. Barnette and S. H. Kim, Effects of surface chemistry on structure and thermodynamics of water layers at solid-vapor interfaces, *J. Phys. Chem. C*, 2009, **113**, 2128–2133.

9 W. Cantrell and G. E. Ewing, Thin film water on muscovite mica, *J. Phys. Chem. B*, 2001, **105**, 5434–5439.

10 W. Cheng, K. Hanna and J. F. Boily, Water Vapor Binding on Organic Matter-Coated Minerals, *Environ. Sci. Technol.*, 2019, **53**, 1252–1257.

11 T. Arai, K. Sato, A. Iida and M. Tomitori, Quasi-stabilized hydration layers on muscovite mica under a thin water film grown from humid air, *Sci. Rep.*, 2017, **7**, 4054.

12 D. Argyris, T. Ho, D. R. Cole and A. Striolo, Molecular dynamics studies of interfacial water at the alumina surface, *J. Phys. Chem. C*, 2011, **115**, 2038–2046.

13 R. Debbarma and A. Malani, Comparative Study of Water Adsorption on a H+ and K+ Ion Exposed Mica Surface: Monte Carlo Simulation Study, *Langmuir*, 2016, **32**, 1034–1046.

14 J. W. Wang, A. G. Kalinichev and R. J. Kirkpatrick, Effects of substrate structure and composition on the structure, dynamics, and energetics of water at mineral surfaces: A molecular dynamics modeling study, *Geochim. Cosmochim. Acta*, 2006, **70**, 562–582.

15 B. Rotenberg, A. J. Patel and D. Chandler, Molecular explanation for why talc surfaces can be both hydrophilic and hydrophobic., *J. Am. Chem. Soc.*, 2011, **133**, 20521–7.

16 A. Hodgson and S. Haq, Water adsorption and the wetting of metal surfaces, *Surf. Sci. Rep.*, 2009, **64**, 381–451.

17 A. Striolo, A. A. Chialvo, K. E. Gubbins and P. T. Cummings, Water in carbon nanotubes: Adsorption isotherms and thermodynamic properties from molecular simulation, *J. Chem. Phys.*, 2005, **122**, 234712.

18 E. Xi, V. Venkateshwaran, L. Li, N. Rego, A. J. Patel, S. Garde and M. L. Klein, Hydrophobicity of proteins and nanostructured solutes is governed by topographical and chemical context, *Proc. Natl. Acad. Sci. U. S. A.*, 2017, **114**, 13345–13350.

19 K. Wada, in *Minerals in soil environments*, eds. J. B. Dixon and S. B. Weed, 1989, pp. 1051–1087.

20 E. Paineau, Imogolite Nanotubes: A Flexible Nanoplatform with Multipurpose Applications, *Appl. Sci.*, 2018, **8**, 1921.

21 G. Monet, E. Paineau, Z. Chai, M. S. Amara, A. Orecchini, M. Jimenéz-Ruiz, A. Ruiz-Caridad, L. Fine, S. Rouzière, L.-M. Liu, G. Teobaldi, S. Rols and P. Launois, Solid wetting-layers in inorganic nano-reactors: the water in imogolite nanotube case, *Nanoscale Adv.*, 2020, **2**, 1869–1877.

22 F. C. Ugolini and R. A. Dahlgren, Weathering environments and occurrence of imogolite and allophane in selected andisols and spodosols, *Soil Sci. Soc. Am. J.*, 1991, **55**, 1166–1171.

23 R. A. Dahlgren and F. C. Ugolini, Formation and stability of imogolite in a tephritic spodosol, Cascade Range, Washington, USA, *Geochim. Cosmochim. Acta*, 1989, **53**, 1897–1904.

24 R. A. Dahlgren and F. C. Ugolini, Distribution and characterization of short-range-order minerals in spodosols from the Washington cascades, *Geoderma*, 1991, **48**, 391–413.

25 C. Levard, E. Doelsch, I. Basile-Doelsch, Z. Abidin, H. Miche, A. Masion, J. Rose, D. Borschneck and J.-Y. Bottero, Structure and distribution of allophanes, imogolite and proto-imogolite in volcanic soils, *Geoderma*, 2012, **183–184**, 100–108.

26 A. G. Jongmans, P. Verburg, A. Nieuwenhuyse and F. Vanoort, Allophane, imogolite and gibbsite in coatings in a Costa-Rican andisol, *Geoderma*, 1995, **64**, 327–342.

27 J. P. Gustafsson, The surface chemistry of imogolite, *Clays Clay Miner.*, 2001, **49**, 73–80.

28 A. Abdelfattah and K. Wada, Adsorption of lead, copper, zinc, cobalt and cadmium by soils that differ in cation-exchange materials, *J. Soil Sci.*, 1981, **32**, 271–283.

29 C. Levard, E. Doelsch, J. Rose, A. Masion, I. Basile-Doelsch, O. Proux, J. L. Hazemann, D. Borschneck and J. Y. Bottero, Role of natural nanoparticles on the speciation of Ni in andosols of la Reunion, *Geochim. Cosmochim. Acta*, 2009, **73**, 4750–4760.

30 S. Rahman, H. Takaki, M. Tamai and Y. Nagatomo, Distribution of zinc, manganese, copper, cobalt, and nickel in Andosols profiles, *Soil Sci. Plant Nutr.*, 1996, **42**, 881–891.

31 M. S. Torn, S. E. Trumbore, O. A. Chadwick, P. M. Vitousek and D. M. Hendricks, Mineral control of soil organic carbon storage and turnover, *Nature*, 1997, **389**, 170–173.

32 P. D. Cradwick, K. Wada, J. D. Russell, Yoshinag.N, C. R. Masson and V. C. Farmer, Imogolite, a hydrated aluminum silicate of tubular structure, *Nature-Physical Sci.*, 1972, **240**, 187-.

33 G. Monet, M. S. Amara, S. Rouzière, E. Paineau, Z. Chai, J. D. Elliott, E. Poli, L.-M. Liu, G. Teobaldi and P. Launois,

Structural resolution of inorganic nanotubes with complex stoichiometry, *Nat. Commun.*, 2018, **9**, 2033.

34 K. Wada and N. Yoshinaga, Structure of imogolite, *Am. Mineral.*, 1969, **54**, 50–71.

35 C. Levard, A. Masion, J. Rose, E. Doelsch, D. Borschneck, C. Dominici, F. Ziarelli and J. Y. Bottero, Synthesis of Imogolite Fibers from Decimolar Concentration at Low Temperature and Ambient Pressure: A Promising Route for Inexpensive Nanotubes, *J. Am. Chem. Soc.*, 2009, **131**, 17080-+.

36 A. Fernandez-Martinez and L. J. Michot, *Physicochemical Properties of Imogolite*, 2016, vol. 7.

37 F. Alvarez-Ramirez, Ab initio simulation of the structural and electronic properties of aluminosilicate and aluminogermanate natotubes with imogolite-like structure, *Phys. Rev. B*, 2007, **76**, 125421.

38 L. Guimaraes, A. N. Enyashin, J. Frenzel, T. Heine, H. A. Duarte and G. Seifert, Imogolite nanotubes: Stability, electronic, and mechanical properties, *ACS Nano*, 2007, **1**, 362–368.

39 E. Balan, M. Lazzeri, G. Morin and F. Mauri, First-principles study of the OH-stretching modes of gibbsite, *Am. Mineral.*, 2006, **91**, 115–119.

40 H. Saalfeld and M. Wedde, Refinement of the crystal structure of gibbsite, Al(OH)3, *Zeitschrift für Krist.*, 1974, **139**, 129–135.

41 R. T. Cygan, J. J. Liang and A. G. Kalinichev, Molecular models of hydroxide, oxyhydroxide, and clay phases and the development of a general force field, *J. Phys. Chem. B*, 2004, **108**, 1255–1266.

42 B. Creton, D. Bougeard, K. S. Smirnov, J. Guilment and O. Poncelet, Molecular dynamics study of hydrated imogolite. 1. Vibrational dynamics of the nanotube, *J. Phys. Chem. C*, 2008, **112**, 10013–10020.

43 B. Creton, D. Bougeard, K. S. Smirnov, J. Guilment and O. Poncelet, Molecular dynamics study of hydrated imogolite - 2. Structure and dynamics of confined water, *Phys. Chem. Chem. Phys.*, 2008, **10**, 4879–4888.

44 B. Creton, D. Bougeard, K. S. Smirnov, J. Guilment and O. Poncelet, Structural model and computer Modeling study of allophane, *J. Phys. Chem. C*, 2008, **112**, 358–364.

45 R. T. Cygan, J. A. Greathouse, H. Heinz and A. G. Kalinichev, Molecular models and simulations of layered materials, *J. Mater. Chem.*, 2009, **19**, 2470–2481.

46 I. C. Bourg, S. S. Lee, P. Fenter and C. Tournassat, Stern Layer Structure and Energetics at Mica-Water Interfaces, *J. Phys. Chem. C*, 2017, **121**, 9402–9412.

47 E. Ferrage, B. A. Sakharov, L. J. Michot, A. Delville, A. Bauer, B. Lanson, S. Grangeon, G. Frapper, M. Jiménez-Ruiz and G. J. Cuello, Hydration properties and interlayer organization of water and ions in synthetic na-smectite with tetrahedral layer charge. Part 2. Toward a precise coupling between molecular simulations and diffraction data, *J. Phys. Chem. C*, 2011, **115**, 1867–1881.

48 H. Zhang and S. J. Singer, Analysis of the subcritical carbon dioxide-water interface, *J. Phys. Chem. A*, 2011, **115**, 6285–6296.

49 E. Veilly, J. Roques, M. C. Jodin-Caumon, B. Humbert, R. Drot and E. Simoni, Uranyl interaction with the hydrated (001) basal face of gibbsite: A combined theoretical and spectroscopic study, *J. Chem. Phys.*, 2008, **129**, 244704.

50 S. Plimpton, Fast parallel algorithms for short-range molecular dynamics, *J. Comput. Phys.*, 1995, **117**, 1–19.

51 D. E. Smith, Molecular computer simulations of the swelling properties and interlayer structure of cesium montmorillonite, *Langmuir*, 1998, **14**, 5959–5967.

52 S.-T. Lin, M. Blanco and W. Goddard, The two-phase model for calculating thermodynamic properties of liquids from molecular dynamics: Validation for the phase diagram of Lennard-Jones fluids, *J. Chem. Phys.*, 2003, **119**, 11792.

53 S.-T. Lin, P. K. Maiti and W. Goddard, Two-phase thermodynamic model for efficient and accurate absolute entropy of water from molecular dynamics simulations., *J. Phys. Chem. B*, 2010, **114**, 8191–8.

54 G. Kresse and J. Hafner, Ab-initio molecular dynamics simulation of the liquid-metal amorphous semiconductor transition in germanium, *Phys. Rev. B*, 1994, **49**, 14251–14269.

55 G. Kresse and J. Hafner, Ab-initio molecular dynamics for liquid metals, *Phys. Rev. B*, 1993, **47**, 558–561.

56 G. Kresse and D. Joubert, From ultrasoft pseudopotentials to the projector augmented-wave method, *Phys. Rev. B*, 1999, **59**, 1758–1775.

57 J. P. Perdew, K. Burke and M. Ernzerhof, Generalized gradient approximation made simple, *Phys. Rev. Lett.*, 1996, **77**, 3865–3868.

58 L. Denaix, I. Lamy and J. Y. Bottero, Structure and affinity towards Cd2+, Cu2+, Pb2+ of synthetic colloidal amorphous aluminosilicates and their precursors, *Colloids Surfaces a-Physicochemical Eng. Asp.*, 1999, **158**, 315–325.

59 A. Noy, D. V. Vezenov and C. M. Lieber, Chemical force microscopy, *Annu. Rev. Mater. Sci.*, 1997, **27**, 381–421.

60 R. W. Friddle, A. Noy and J. J. De Yoreo, Interpreting the widespread nonlinear force spectra of intermolecular bonds., *Proc. Natl. Acad. Sci. U. S. A.*, 2012, **109**, 13573–8.

61 S. A. Gazze, I. Hallin, G. Quinn, E. Dudley, G. P. Matthews, P. Rees, G. Van Keulen, S. H. Doerr and L. W. Francis, Organic matter identifies the nano-mechanical properties of native soil aggregates, *Nanoscale*, 2018, **10**, 520–525.

62 T. Hassenkam, L. L. Skovbjerg and S. L. S. Stipp, Probing the intrinsically oil-wet surfaces of pores in north sea chalk at subpore resolution, *Proc. Natl. Acad. Sci. U. S. A.*, 2009, **106**, 6071–6076.

63 P. D. Ashby and C. M. Lieber, Ultra-sensitive imaging and interfacial analysis of patterned hydrophilic SAM surfaces using energy dissipation chemical force microscopy, *J. Am. Chem. Soc.*, 2005, **127**, 6814–6818.

64 W. Fu and W. Zhang, Measurement of the surface hydrophobicity of engineered nanoparticles using an atomic force microscope, *Phys. Chem. Chem. Phys.*, 2018, **20**, 24434–24443.

65 P. Stock, J. I. Monroe, T. Utzig, D. J. Smith, M. S. Shell and M. Valtiner, Unraveling Hydrophobic Interactions at the Molecular Scale Using Force Spectroscopy and Molecular Dynamics Simulations, *ACS Nano*, 2017, **11**, 2586–2597.

66 O. Dudko, G. Hummer and A. Szabo, Intrinsic Rates and Activation Free Energies from Single-Molecule Pulling Experiments, *Phys. Rev. Lett.*, 2006, **96**, 108101.

67 J. L. Hutter and J. Bechhoefer, Calibration of atomic-force microscope tips, *Rev. Sci. Instrum.*, 1993, **64**, 1868–1873.

68 R. W. Friddle, K. Battle, V. Trubetskoy, J. Tao, E. A. Salter, J. Moradian-Oldak, J. J. De Yoreo and A. Wierzbicki, Single-molecule determination of the face-specific adsorption of Amelogenin's C-terminus on hydroxyapatite., *Angew. Chem. Int. Ed. Engl.*, 2011, **50**, 7541–5.

69 T. D. Kühne and R. Z. Khaliullin, Electronic signature of the instantaneous asymmetry in the first coordination shell of liquid water, *Nat. Commun.*, 2013, **4**, 1–7.

70 G. Desiraju and T. Steiner, *The Weak Hydrogen Bond In Structural Chemistry and Biology*, Oxford Scholarship Online, Oxford, UK, 2010.

71 D. T. Limmer, A. P. Willard, P. Madden and D. Chandler, Hydration of metal surfaces can be dynamically heterogeneous and hydrophobic, *Proc. Natl. Acad. Sci. U. S. A.*, 2013, **110**, 4200–4205.

72 M. L. Machesky, M. Predota, D. J. Wesolowski, L. Vlcek, P. T. Cummings, J. Rosenqvist, M. K. Ridley, J. D. Kubicki, A. V Bandura, N. Kumar and J. O. Sofo, Surface Protonation at the Rutile (110) Interface: Explicit Incorporation of Solvation Structure within the Refined MUSIC Model Framework, *Langmuir*, 2008, **24**, 12331–12339.

73 I. D. Brown and D. Altermatt, Bond-valence parameters obtained from a systematic analysis of the Inorganic Crystal-Stucture Database, *Acta Crystallogr. Sect. B-Structural Sci.*, 1985, **41**, 244–247.

74 G. Sposito, *The surface chemistry of natural particles*, Oxford University Press, New York, 1st edn., 2004.

75 T. Hiemstra and W. H. VanRiemsdijk, A surface structural approach to ion adsorption: The charge distribution (CD) model, *J. Colloid Interface Sci.*, 1996, **179**, 488–508.

76 Y. Arai, M. McBeath, J. R. Bargar, J. Joye and J. A. Davis, Uranyl adsorption and surface speciation at the imogolite-water interface: Self-consistent spectroscopic and surface complexation models, *Geochim. Cosmochim. Acta*, 2006, **70**, 2492–2509.

77 D. A. Sverjensky, Prediction of surface charge on oxides in salt solutions: Revisions for 1 : 1 (M+L-) electrolytes, *Geochim. Cosmochim. Acta*, 2005, **69**, 225–257.

78 T. Hiemstra, P. Venema and W. H. VanRiemsdijk, Intrinsic proton affinity of reactive surface groups of metal (hydr)oxides: The bond valence principle, *J. Colloid Interface Sci.*, 1996, **184**, 680–692.

79 T. Hiemstra, H. Yong and W. H. Van Riemsdijk, Interfacial charging phenomena of aluminum (Hydr)oxides, *Langmuir*, 1999, **15**, 5942–5955.

80 Y. Gan and G. V Franks, Charging behavior of the Gibbsite basal (001) surface in NaCl solution investigated by AFM colloidal probe technique, *Langmuir*, 2006, **22**, 6087–6092.

81 B. R. Bickmore, C. J. Tadanier, K. M. Rosso, W. D. Monn and D. L. Eggett, Bond-valence methods for pKa prediction: critical reanalysis and a new approach, *Geochim. Cosmochim. Acta*, 2004, **68**, 2025–2042.

82 I. D. Brown, *The Chemical Bond in Inorganic Chemistry: The Bond Valence Model*, Oxford University Press, New York, 2002.

83 B. R. Bickmore, K. M. Rosso, I. D. Brown and S. Kerisit, Bond-Valence Constraints on Liquid Water Structure, *J. Phys. Chem. A*, 2009, **113**, 1847–1857.

84 I. Basile-Doelsch, R. Amundson, W. E. E. Stone, C. A. Masiello, J. Y. Bottero, F. Colin, F. Masin, D. Borschneck and J. D. Meunier, Mineralogical control of organic carbon dynamics in a volcanic ash soil on La Reunion, *Eur. J. Soil Sci.*, 2005, **56**, 689–703.

85 T. Chevallier, T. Woignier, J. Toucet, E. Blanchart and P. Dieudonne, in *14th International Sol-Gel Conference*, Montpellier, FRANCE, 2007, pp. 231–238.

86 M. Egli, M. Nater, A. Mirabella, S. Raimondi, M. Ploetze and L. Alioth, Clay minerals, oxyhydroxide formation, element leaching and humus development in volcanic soils, *Geoderma*, 2008, **143**, 101–114.

87 B. K. G. Theng and G. D. Yuan, Nanoparticles in the Soil Environment, *Elements*, 2008, **4**, 395–399.

88 M. A. Wilson, N. H. Tran, A. S. Milev, G. S. K. Kannangara, H. Volk and G. Q. M. Lu, Nanomaterials in soils, *Geoderma*, 2008, **146**, 291–302.

89 C. Rasmussen, K. Heckman, W. R. Wieder, M. Keiluweit, C. R. Lawrence, A. A. Berhe, J. C. Blankinship, S. E. Crow, J. L. Druhan, C. E. Hicks Pries, E. Marin-Spiotta, A. F. Plante, C. Schädel, J. P. Schimel, C. A. Sierra, A. Thompson and R. Wagai, Beyond clay: towards an improved set of variables for predicting soil organic matter content, *Biogeochemistry*, 2018, **137**, 297–306.

90 D. Spagnoli, J. F. Banfield and S. C. Parker, Free energy change of aggregation of nanoparticles, *J. Phys. Chem. C*, 2008, **112**, 14731–14736.

91 D. Li, M. H. Nielsen, J. R. I. Lee, C. Frandsen, J. F. Banfield and J. J. De Yoreo, Direction-specific interactions control crystal growth by oriented attachment, *Science (80-.).*, 2012, **336**, 1014–1018.